Chapter 16
Large Scale Testing Facilities – Use of High Gravity Centrifuge Tests to Investigate Soil Liquefaction Phenomena

Gopal S. P. Madabhushi

Abstract Soil liquefaction following earthquake events causes severe damage to Civil Engineering Infrastructure as witnessed in many of the recent earthquake events. High gravity centrifuge tests are able to simulate earthquake induced liquefaction in saturated soils and allow us to study the physics behind liquefaction phenomena and the behaviour of structures that are located on such sites. In this paper, the use of large scale testing facilities in studying the problems in geotechnical earthquake engineering will be highlighted. Soil liquefaction problems are used as a vehicle to illustrate the use of these large scale testing facilities. Some of the recent investigations that were carried out at University of Cambridge will be presented. These include the novel testing that was carried out which involved creation of triaxial chambers within centrifuge models to delineate drainage effects on liquefiable soils. Direct comparisons are made between free-field soil and the soil enclosed within the triaxial chamber. Similarly the reduction in settlement of foundations on liquefiable soils due to air injection *a priori* to earthquake loading will be presented. The differences in the failure mechanisms of shallow foundations caused by the injected air are presented.

16.1 Large Scale Testing Facilities

In geotechnical earthquake engineering, it is very attractive to conduct large scale testing of physical models to understand the failure mechanisms created by earthquake loading in a specific boundary value problem such as retaining walls, pile foundations or embankment dam failures. As the soil exhibits highly non-linear behaviour under the action of earthquake loading which begets large stresses and large strains, it is imperative that the physical models are tested at prototype stresses and strains. A convenient way to generate full scale, prototype stresses and strains in

G. S. P. Madabhushi (✉)
Professor of Civil Engineering, University of Cambridge, Cambridge, UK
e-mail: mspg1@cam.ac.uk

359

Fig. 16.1 A view of the 10 m diameter Turner Beam Centrifuge at University of Cambridge

small scale physical models is by the use a high gravity centrifuge, such as the one at the Schofield Centre, University of Cambridge, shown in Fig. 16.1. This is a balanced beam geotechnical centrifuge that is classified as 150 g-ton machine with a payload capacity of about 1 ton. For earthquake simulation tests the maximum centrifugal acceleration is restricted to about 100 g's. The principles of centrifuge modelling are described later in Sec. 2.

16.1.1 Earthquake Actuators

In order to model earthquake loading on centrifuge models in-flight, powerful earthquake actuators are required. These actuators need to deliver large forces (of the order of several kN) in a very short time scale (of the order of fractions of seconds) due to the scaling laws presented later in Table 16.1. In Cambridge there are two types of earthquake actuators that are available to the modellers. These are described next.

16.1.1.1 Stored Angular Momentum (SAM) Earthquake Actuator

Much of the research in the last decade in Cambridge in the area of earthquake geotechnical engineering has been carried out using the Stored Angular Momentum (SAM) actuator. This device was developed by Madabhushi et al. (1998) and shown in Fig. 16.2. SAM actuator has been prolific over the last decade and produced more than 10 PhD theses. The SAM actuator operates by storing all the required energy for firing a model earthquake in a set of fly wheels, which are spun up to the required RPM using a 3 phase electric motor. The fly wheels have the stored angular momentum at the frequency of the required earthquake. The fly wheels are enclosed in a crank case and drive a reciprocating rod. A fast acting clutch was developed at Cambridge that can engage the reciprocating rod in under 20 ms. When an earthquake is desired, the fast acting clutch is activated by using high pressure nitrogen. This engages the shaking table on which the centrifuge model package is mounted. The magnitude of the earthquake can be adjusted by moving the pivot point on the

Table 16.1 Scaling laws

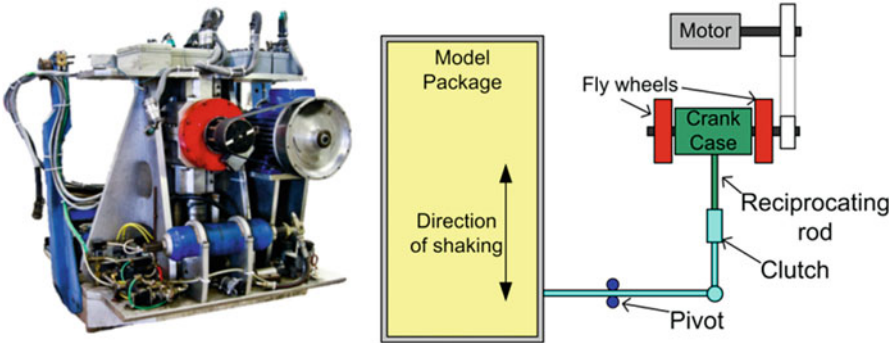|	Parameter	Scaling law model/prototype
General scaling laws (slow events)	Length	1/N
	Area	$1/N^2$
	Volume	$1/N^3$
	Mass	$1/N^3$
	Stress	1
	Strain	1
	Force	$1/N^2$
	Work	$1/N^3$
	Energy	$1/N^3$
	Seepage velocity	N
	Time (consolidation)	$1/N^2$
Dynamic events	Time (dynamic)	1/N
	Frequency	N
	Displacement	1/N
	Velocity	1
	Acceleration /	N
	Acceleration due}	
	To gravity (g's)	

Fig. 16.2 A view of the Stored Angular Momentum (SAM) earthquake actuator

cross rod. Thus the frequency, duration and intensity of the model earthquakes can be chosen by the centrifuge modeller. An example of a typical earthquake that has been produced by the SAM actuator is shown in Fig. 16.3. In this example, the centrifuge modeller fired the earthquake in a 50 g test at a frequency of 40 Hz. The duration of the earthquake was chosen as 500 ms. In Fig. 16.3 the equivalent prototype earthquake is shown which has a magnitude of about 0.2 g applied at the base of the model (i.e. bedrock motion). The FFT of the motion in Fig. 16.3 shows that most of the energy of the earthquake is concentrated at 0.8 Hz although a higher harmonic is present at 2.1 Hz. The duration of the prototype earthquake is

Fig. 16.3 An example of
the sinusoidal input motion
from SAM actuator
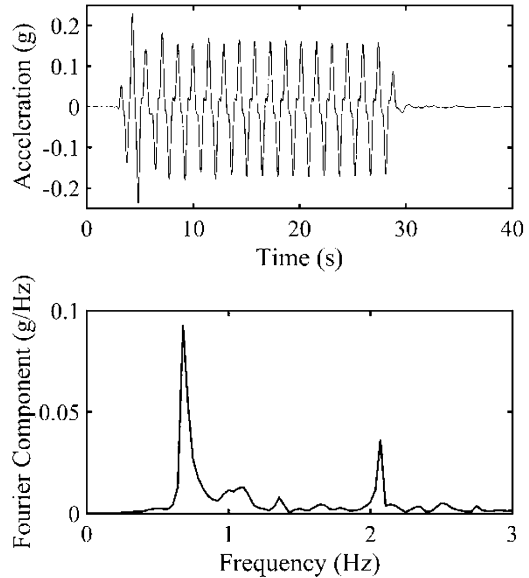
about 25 s. The dynamic scaling laws presented in Table 16.1 were used to convert
the model earthquake characteristics into an equivalent prototype event.

SAM actuator is a simple, mechanical actuator that is economical to build and has
operated reliably for over a decade. However, it has certain limitations. For example,
it can produce sinusoidal or swept sine wave motions only.

16.1.1.2   Servo-Hydraulic Earthquake Actuator

The main advantage of a servo-hydraulic earthquake actuator is that it offers the
researchers opportunity to simulate real earthquake motions. These servo-controlled
actuators are able to vary the amplitude and frequency content of earthquake motion
applied to the centrifuge models.

In Cambridge a new servo-hydraulic shaker has been developed that was
commissioned in late 2011. Madabhushi et al. (2012) describe the construction
and performance of this actuator. A view of this earthquake actuator is shown in
Fig. 16.4. The main operating principle of this earthquake actuator is that the energy
required to fire the model earthquakes is stored in highly pressurised hydraulic oil.
The hydraulic oil is pressurised to about 260 bar and pumped into four main
accumulators. The pressurised oil is then directed through a double acting actuator
directly attached to the shake table. The spent oil is then collected in a low pressure
(7 bar) accumulator. The movement of the double acting actuator is servo-controlled
through a close loop by the servo-amplifier.

The servo-hydraulic earthquake actuator built at Cambridge uses many of the
features of the Turner beam centrifuge shown in Fig. 16.1. For example, the main

Fig. 16.4 A view of the
Servo-Hydraulic
Earthquake Actuator

reaction to the earthquake shaking force imparted to the centrifuge model will be
provided by the main body of the beam centrifuge. The entire shaker assembly is
mounted on a self-contained swing which can be loaded and unloaded like any other
centrifuge package tested on the centrifuge. The hydraulic power pack that supplies
the high pressure fluid is outside the centrifuge and is supplied to the earthquake
actuator through high pressure fluid slip rings.

One of the main advantages of using a servo-hydraulic earthquake actuator is that
we can simulate more realistic motions as mentioned earlier. In Fig. 16.5a an
example input motion generated by the servo-hydraulic earthquake actuator in a
50 g centrifuge test to simulate a scaled Kobe earthquake motion of 1995 is
presented. The peak amplitude of the input motion in this case was about 0.2 g
and the duration of the earthquake was about 12 s. In this figure the FFT of the input
motion is also presented which shows the presence of multiple peaks corresponding
to the frequency components in the earthquake motion. Similarly in Fig. 16.5b an
example of the input motion of the Imperial Valley motion in a 50 g centrifuge test is
presented. This motion is much longer i.e. nearly 80 s in prototype scale. The FFT of
this input motion also shows the high frequency content of this motion captured by
the servo-hydraulic earthquake actuator.

16.1.2 Model Containers

Dynamic centrifuge modelling requires the use of specialist model containers. As the
centrifuge models are subjected to earthquake motions at the base, the ends of the
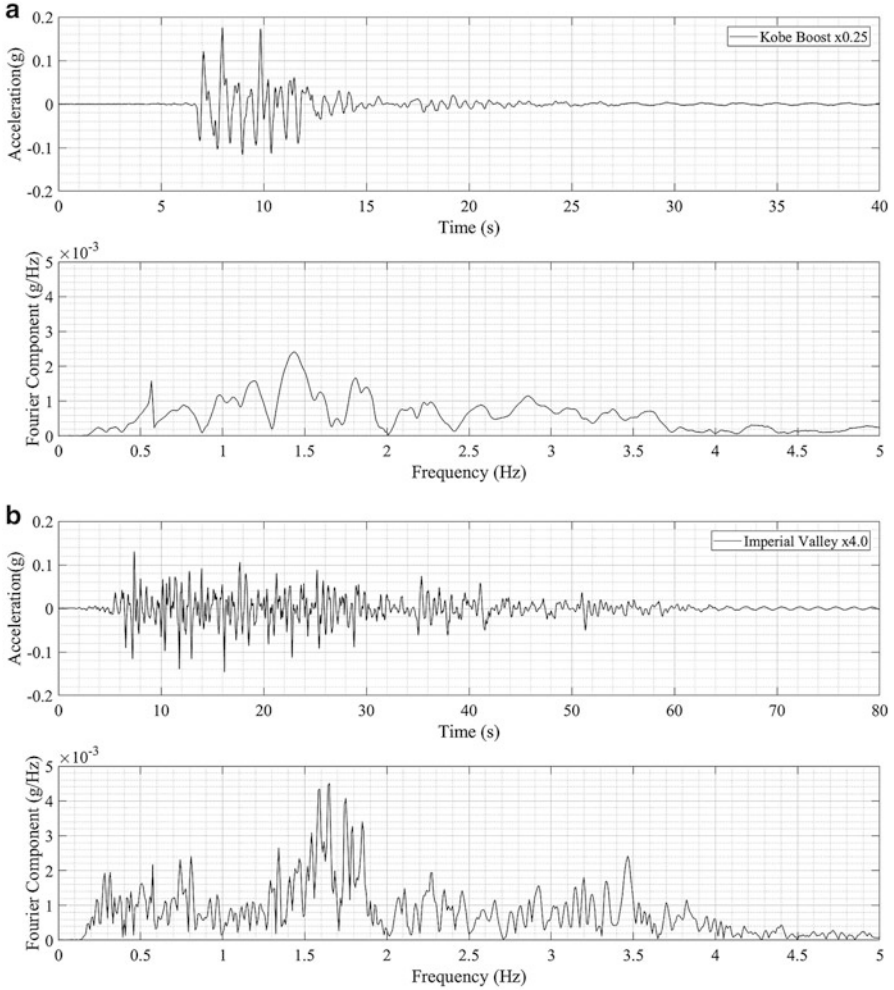container, if rigid, can impose additional, spurious P waves in the soil body. Several

Fig. 16.5 Example input motions generated by the Servo-Hydraulic earthquake actuator (**a**) Kobe Earthquake motion (**b**) Imperial Valley motion

researchers have focused on developing specialised model containers that reduce the impact of these P waves from the end walls of the container.

16.1.2.1 Laminar Model Container

One concept is to use laminae that are separated by cylindrical bearings that allow free displacement of each lamina relative to the next. Such containers undergo free,
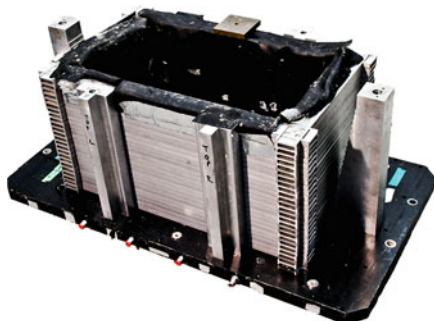
Fig. 16.6 Laminar model container

**Fig. 16.7** Equivalent Shear Beam Model container

lateral displacement allowing the soil lateral movements of the soil. A view of the Cambridge laminar box is shown in Fig. 16.6. This container is able to model a depth of about 25 m of soil depth in a 80 g centrifuge test. More details of the laminar box and its performance is described by Brennan et al. (2006). The most effective use of laminar model container is in modelling of lateral spreading problems following soil liquefaction. As the container has effectively no stiffness laterally, it is able to deform following the spreading of the liquefied soil on a slope.

16.1.2.2 Equivalent Shear Beam (ESB) Model Container

Another concept of model container is to mimic the lateral deformations observed in a free, vertical column of soil modelled as a shear beam. The lateral deflections in the soil are calculated for a given magnitude earthquake. These are matched by constructing the equivalent shear beam (ESB) container with alternating rings of aluminium and rubber. The thickness of the rubber can be changed with the depth of the model container. A view of one the ESB model containers at Cambridge is shown in Fig. 16.7. This containers construction and performance are described in detail by Zeng and Schofield (1996). This container is able to model a depth of about 16 m of soil in a 80 g test. Larger ESB model containers were also constructed at Cambridge, which follow the same design principle, but can model depths of about 34 m in a 80 g centrifuge test. The ESB model containers are useful in modelling level ground problems to study soil structure interaction, for example.

Fig. 16.8 Transparent
sided model container with a
45° mirror
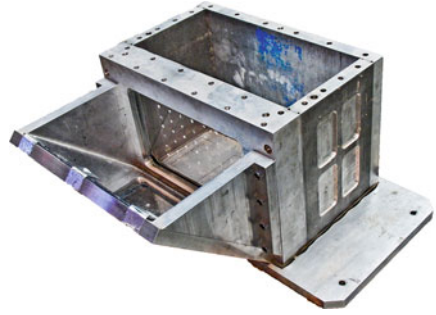
16.1.2.3 Transparent Sided Model Container

While the above model container simulate the free-field conditions well in specific centrifuge tests, they have the disadvantage of being opaque when viewed from the side. With the recent advances in high speed imaging and the development of the geo-PIV software (White et al. 2003), it is now possible to obtain high resolution images using high speed cameras that can acquire images at 1000 frames per second. However, this requires the side of the model containers to be transparent. Initial attempts at using high speed cameras in dynamic centrifuge testing were carried out by Cilingir and Madabhushi (2011) using a transparent sided model container shown in Fig. 16.8. This set up used a vertically mounted Phantom Camera and a 45° mirror and was quite successful in obtaining soil displacements and soil strains during earthquake loading next to model tunnels.

More recently, a more compact Motion Blitz cameras became available, that can be mounted directly in front of the transparent window and removing the need for the 45° mirror.

16.2 Principle of Centrifuge Modelling

The basic premise in centrifuge modelling is that we test 1/N scale model of a prototype in the enhanced gravity field of a geotechnical centrifuge (Madabhushi 2014). The gravity is increased by the same geometric factor N relative to the normal earth's gravity field.

This can be illustrated using a simple example. Let us consider a block structure of mass M and with dimensions $L \times B \times H$ sited on a horizontal soil bed as shown in Fig. 16.9. The average vertical stress exerted by this block on the soil can be easily calculated as;

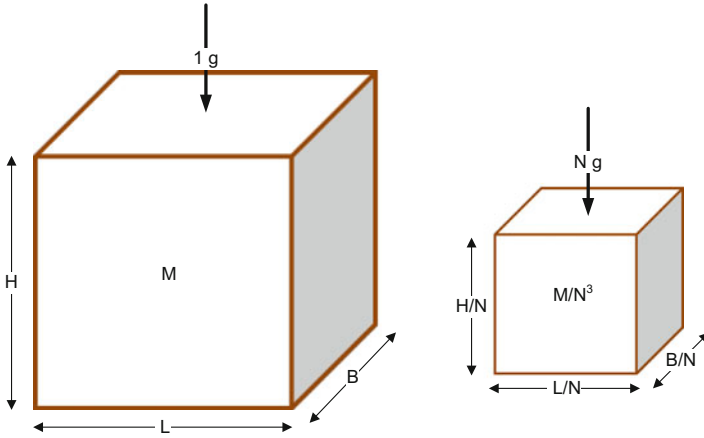$$\sigma_v = \frac{M\,g}{L \times B} \tag{16.1}$$

Fig. 16.9 Principle of centrifuge modelling

Similarly the vertical strain induced in the soil at any given point can be calculated as;

$$\varepsilon = \frac{\delta\alpha}{\alpha} \tag{16.2}$$

where α is a characteristic length in the soil body. Now let us consider a scale model of this block in which all the dimensions are scaled down by a factor N as shown in Fig. 16.1. As all the dimensions are scaled down by a factor N, the mass of this scaled down block will be M/N^3. Let us now imagine that this scale model of the block is placed in the increased gravity field of $N \times$ earth's gravity. If we now recalculate the vertical stress underneath this scale model of the block, we can see that;

$$\sigma_v = \frac{\frac{M}{N^3} \times Ng}{\frac{L}{N} \times \frac{B}{N}} = \frac{M}{L \times B}\frac{g}{} \tag{16.3}$$

Thus the vertical stress below this scale model of the block is same as that below the larger block obtained in Eq. 16.1.

Similarly, if we consider strains in the soil;

$$\varepsilon = \frac{\delta\alpha}{\Big/ \frac{N}{\alpha/N = \frac{\delta\alpha}{\alpha}}} \tag{16.4}$$

we can see that the prototype strain in Eq. 16.2 is recovered, as the changes in displacements and the original length are both scaled by the same factor N.

We increase the 'gravity' acting on our scaled model by placing it in a geotechnical centrifuge. The centrifugal acceleration will give us the 'N g' environment in which the scaled model will behave in an identical fashion to the prototype in the field. We can relate the angular velocity of the centrifuge to the required 'g' level.

When the centrifuge is rotating with an angular velocity of $\dot{\theta}$, the centrifugal acceleration at any radius 'r' is given by;

$$\bar{a} = r\,\dot{\theta}^2 \tag{16.5}$$

We wish to match this centrifugal acceleration to be the same geometric scale factor as the one we used to scale down our prototype by i.e. N.

$$N\,g = r\,\dot{\theta}^2 \tag{16.6}$$

The centrifugal acceleration changes with the radial distance from the axis of rotation of the centrifuge as indicated in Eq. 16.6. We will normally arrange the speed of the centrifuge such that the model at the desired radius (say a typical point in the model like its centroid) will experience the desired centrifugal acceleration 'Ng'. This will give us the angular velocity $\dot{\theta}$ with which we have to rotate our centrifuge. For example, for the Turner beam centrifuge at Cambridge the nominal working radius is 4.125 m. If we need to create a centrifugal acceleration of '100 g' on a centrifuge model, then using Eq. 16.6, we can calculate the angular velocity as;

$$\dot{\theta} = \sqrt{\frac{100 \times 9.81}{4.125}} = 15.42 \ rad/s$$

$$\dot{\theta} = 147.3 \ RPM \tag{16.7}$$

So by spinning the centrifuge at 147.3 RPM, we can create the required 100 g of centrifugal acceleration.

In centrifuge modelling the model behaviour observed during testing must be related to the behaviour of the equivalent field sized structure. This is achieved by a set of scaling laws that link the model and prototype parameters. The scaling laws were originally proposed by Schofield (1980, 81) and are easy to derive as shown by Madabhushi (2014). A set of important scaling laws are reproduced in Table 16.1.

In Table 16.1 it is seen that the scaling law for dynamic events are somewhat different from those for slower general events. For example, the scaling for dynamic time and consolidation time differ by a factor of 1/N. This conflict in model scales is normally avoided by scaling the viscosity of pore fluid (Adamidis and Madabhushi 2015). Depending on the type of problem being modelled, centrifuge modellers are able to make suitable adjustments to the models to capture the most representative prototype behaviour.

16.3   Soil Liqueafaction

In this paper soil liquefaction is used as an example of a complex problem that can be modelled effectively using centrifuge modelling. Many of the recent earthquakes have caused extensive damage to infrastructure due to soil liquefaction. Some examples of these are presented below.

16.3.1 Examples of Soil Liquefaction

There are many examples of damage to civil engineering structures due to soil liquefaction. The settlement and rotation of the Harbour Master's tower at Kandla port due to soil liquefaction is shown in Fig. 16.10 following the Bhuj earthquake of 2001. This building was supported on pile foundations that pass through a soil profile that is susceptible to liquefaction. Further details of this case history can be found in Madabhushi et al. (2005). A similar failure mechanism was observed in New Zealand earthquake of 2011 in the case of a low-rise residential building supported on shallow foundations shown in Fig. 16.10. Here the super-structure showed very little damage but the building was a write-off due to foundation failure. Madabhushi and Haigh (2009) argued that the super-structure stiffness plays an important role in determining the failure mechanism of the structure located on liquefiable soil. In Fig. 16.11 the lateral spreading caused by soil liquefaction in Portoveijo in the recent Ecuador earthquake is presented. Soil liquefaction and subsequent lateral spreading causes a different type of failure in pile foundations. During the Haiti earthquake, the pile foundations of a wharf structure in Port au Prince suffered formation of plastic hinges at pile heads as shown in Fig. 16.11. A similar mechanism was proposed *a priori* based on dynamic centrifuge model tests by Knappett and Madabhushi (2009) also shown as an inset in Fig. 16.11.

On the other hand, underground structures like tunnels, pipe lines or fluid storage tanks (when partially empty) are naturally buoyant structures. Soil liquefaction can cause floatation of such structures. During the Tohuku earthquake of Japan, an underground tank has suffered floatation as shown in Fig. 16.12. Chian et al.

Fig. 16.10 Settlement and rotation of a tall structure and a residential structure due to soil liquefaction

Fig. 16.11 Lateral spreading due to soil liquefaction and damage to pile foundations

Fig. 16.12 Flotation of an underground tank following soil liquefaction

(2014) investigated the effects of floatation of underground structures due to soil liquefaction in detail.

Although all these failures are different, the underlying cause of their predicament is soil liquefaction. The last two decades have seen a great advancement of both the scientific understanding of liquefaction phenomena and of modelling liquefaction using numerical and centrifuge modelling, particularly with the establishment of the George E Brown Network of Earthquake Engineering Simulation (NEES) in the USA and similarly the UK-NEES network. The failure mechanisms of buildings, piles, retaining walls and bridge foundations have been widely investigated. Despite these advancements, there are several aspects of liquefaction that remain unclear. The definition of liquefaction may be considered as a specific example. Soil lique-faction may be defined, using Terazaghi's effective stress principle, as the state of saturated soils when the pore pressure matches the total stress, thereby reducing the effective stress to zero.

$$\sigma'_v = \sigma_v - (u_{hyd} + u_{excess}) \tag{16.8}$$

where u_{hyd} and u_{excess} are hydrostatic and excess pore pressures respectively. The total stress σ_v, is usually considered to be the geostatic vertical stress. This definition is appropriate for level ground with no buildings or other structures. When considering a soil element below a building, the total stress in the soil is affected by the bearing pressure exerted by the building and therefore a higher excess pore pressure may be required to liquefy the soil. This is, however, difficult to determine, as the stress distribution due to the structure changes with the onset of liquefaction. Coelho et al. (2007) show that the stress distribution below a shallow foundation narrows down with liquefaction, forming a column of highly stressed soil underneath the foundation that remains non-liquefied while the free field soil fully liquefies. Similar observations were also made by Ghosh and Madabhushi (2007), who investigated excess pore pressure generation underneath a heavy foundation for a nuclear reactor building. Underneath a building, the vertical effective stress therefore changes with the evolution of excess pore pressures generated by earthquake loading from two viewpoints. Firstly, using Eq. 16.8, the effective stress decreases as excess pore pressures increase. Secondly, the change in stress distribution below the building causes the total and hence effective stresses to change. Thus the definition of liquefaction, given earlier, needs to be updated. It must be understood that the value of effective stress in Eq. 16.8 is not the free field effective stress or the initial effective stress. It must be the effective stress at any given point and at any given time, where the excess pore pressure is known. It must also be pointed out that in this paper the subtle differences between 'initial liquefaction' and 'flow liquefaction' (Kramer 1996) have not been considered.

16.3.2 Theoretical Framework of Liquefaction

Casagrande (1936) proposed the existence of a 'critical void ratio' for sands, based on his load-controlled drained shear box tests. He envisaged that when a natural soil deposit has a void ratio equals to or greater than this 'critical void ratio', it is susceptible to liquefaction failure. Casagrande (1971) described the observation of liquefaction in undrained cyclic loading of saturated sands in triaxial tests as the point at which there is a substantial loss of shear strength when the sand is subjected to continuous shear strains. Further, he described the point at which the pore pressure in the sample equals the cell pressure in a cyclic triaxial test on a dense sand sample as 'cyclic mobility'. Castro (1969) associated liquefaction with a sudden loss of shear strength resulting in a catastrophic failure. In laboratory tests, he observed that a sample of sand subjected to cyclic or monotonic loading exhibited liquefaction failure only if the driving stresses were larger than the undrained shear strength of the sample. Following earthquake loading and the subsequent generation of excess pore pressures in saturated sands, the driving shear stresses below a building can be greater than the undrained shear strength. Castro considered the steady state deformations that occur in the presence of elevated pore pressures following earthquake loading as liquefaction failure. This was thought to be justified, as many dams such

as the upper and lower San Fernando dams were known to have failed after the end of earthquake loading, (Dixon and Burke 1973). Dixon and Burke observed that there was a possibility of liquefaction occurring at great depths below these dams contrary to the opinion of Casagrande (1971).

Roscoe et al. (1958) and Schofield and Wroth (1968) established the Critical State soil mechanics framework based on the postulation that a soil element that has reached a Critical State will continuously deform without further changes in stress or volume. This state can be depicted as a single line in q-p′-v space. Schofield (1980, 1981) and later Muhunthan and Schofield (2000) applied the Critical State framework to soil liquefaction. Consider the stress state of a soil element on the loose or 'wet' side of the Critical State. When this soil element is subjected to cyclic shear stresses under undrained conditions, the propensity to suffer volumetric contraction is manifested as an increase in excess pore water pressures. This causes the effective confining stress to reduce, as shown in Fig. 16.13. Eventually, the stress path will cross the tensile rupture or fracture surface resulting in a disaggregation of the continuum into a clastic body with unstressed grains free to slide apart. This results in the massive loss of strength seen during liquefaction.

One of the manifestations of the soil stress path reaching the fracture surface shown in Fig. 16.13 is that the soil permeability increases at these very low effective stresses. Haigh et al. (2012) demonstrated that this is possible based on simple soil column experiments with upward hydraulic gradients causing fluidization of sand layer and resulting in near 'liquefaction' state with very low vertical effective stresses. It must be pointed out that in these experiments there was no earthquake induced shear stress that causes excess pore water pressures. However the loss of effective stress due to upward hydraulic gradients is considered to take the soil's stress path into the same low effective stress regime as that of an earthquake induced soil liquefaction state. In Fig. 16.14 the changes in permeability with effective stresses are presented for three different types of sands. The increased permeability for effective stress values of <0.2 kPa can be clearly seen in this figure. In addition it can be seen in Fig. 16.14 that the finer soils such as Fraction E sand show a larger reduction in the permeability in this low effective stress range compared to relatively coarser grained sands such as Fraction D or Hostun sand. In addition to the changes

Fig. 16.13 Critical State framework for soil liquefaction. (After Muhunthan and Schofield 2000)
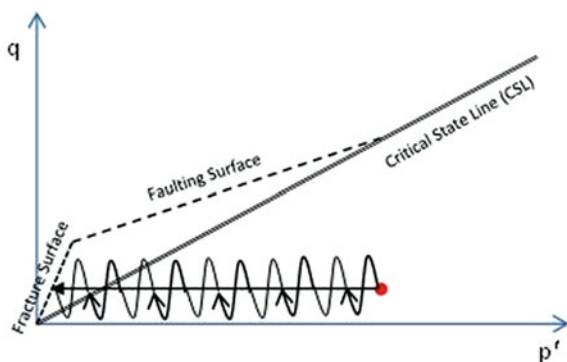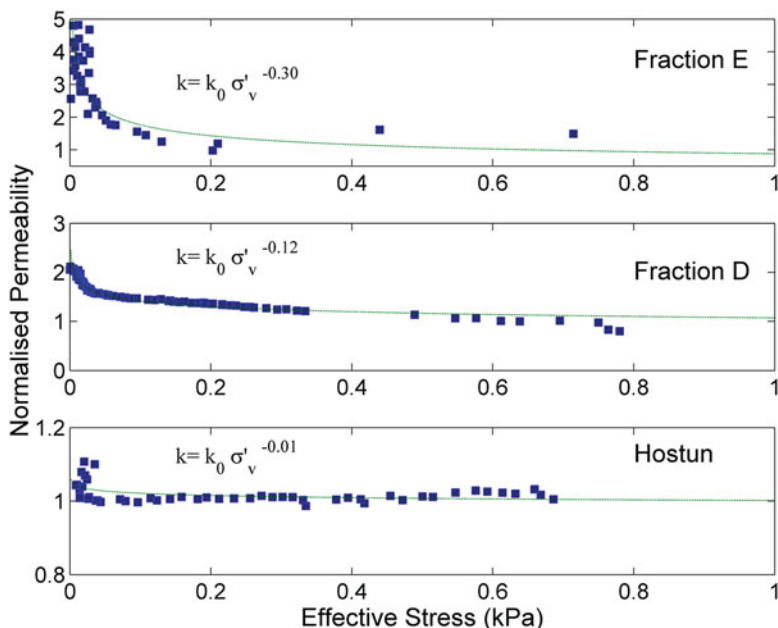
**Fig. 16.14** Change in permeability at low effective stresses

in permeability of sands, at very low effective stresses their compressibility also changes. More details on this aspect are discussed by Haigh et al. (2012) and by Adamidis and Madabhushi (2016).

16.4 Dynamic Centrifuge Testing of Soil Liquefaction Problems

16.4.1 Simple, Level Sand Beds

Dynamic centrifuge tests were carried out on loose and dense sand layers by Coelho et al. (2007). These were horizontal, fully saturated sand beds tested at 50 g with prototype dimensions of 33.6 m long and 18.2 m deep. The soil used was uniformly graded Fraction E sand (Leighton Buzzard 100/170). This silica sand was extensively used in many research projects at Cambridge and its properties are well established. While the models were heavily instrumented as reported by Coelho et al., in this paper only three instruments will be considered as shown in Fig. 16.15. These will be the base accelerometer (ACC) that records the input acceleration, a pore pressure transducer (PPT) at a depth of 14.6 m (292 mm at model scale) that

Fig. 16.15 Cross-sectional
view of the centrifuge model
in an ESB model container
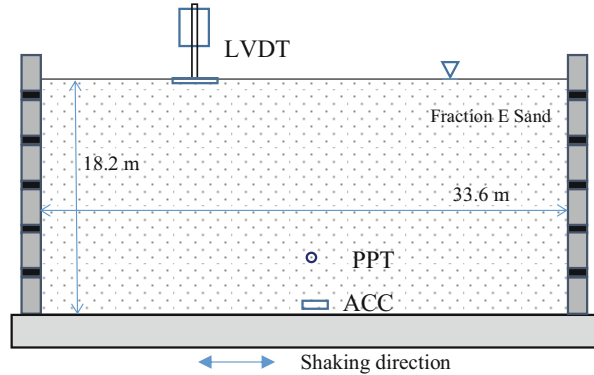
records excess pore pressures and a surface LVDT that measures soil settlement.
Again only two tests with relative density of soil model of 50% (loose) and 80%
(dense) will be considered here, although more tests were carried out at intermediate
relative densities, Coelho et al. (2007) (Fig. 16.15).

In Figs. 16.16 and 16.17, the results from dynamic centrifuge tests on soil
deposits with relative densities of 50% and 80% are presented. Both models were
subjected to very similar earthquake loading with a peak horizontal acceleration of
5 g with nominally 10 cycles. This peak acceleration of 5 g is equivalent to 0.2 g of
peak acceleration applied at the bedrock level at prototype scale.

16.4.1.1 Excess Pore Pressures

In Fig. 16.16, it can be seen that both soil models experience excess pore water
pressures of about 140 kPa, equivalent to the total vertical stress at the depth of the
instrument. This $\sigma_v = u_{excess}$ line is plotted in these figures as a dashed line to
indicate soil liquefaction following the definition given by Eq. 16.1. The main
difference in the excess pore pressure traces is that for the case of dense sand
shown in Fig. 16.16b, the dilation is stronger, manifested as larger amplitude suction
cycles being superposed on the excess pore pressure generated. It may also be noted
that during these large suction cycles, the excess pore pressure temporarily exceeds
the dashed line suggesting that the excess pore pressures are greater than the total
stress for those brief moments. This is only possible if vertical equilibrium is not
maintained at those moments, i.e. the soil body has to accelerate vertically upwards.
Further it can be seen in Fig. 16.16 that the soil starts to reconsolidate after the end of
earthquake as the excess pore pressures slowly start to dissipate. The rates of excess
pore pressure dissipation are very similar for both loose and dense sands. Brennan
and Madabhushi (2011) showed that the co-efficient of consolidation can be calcu-
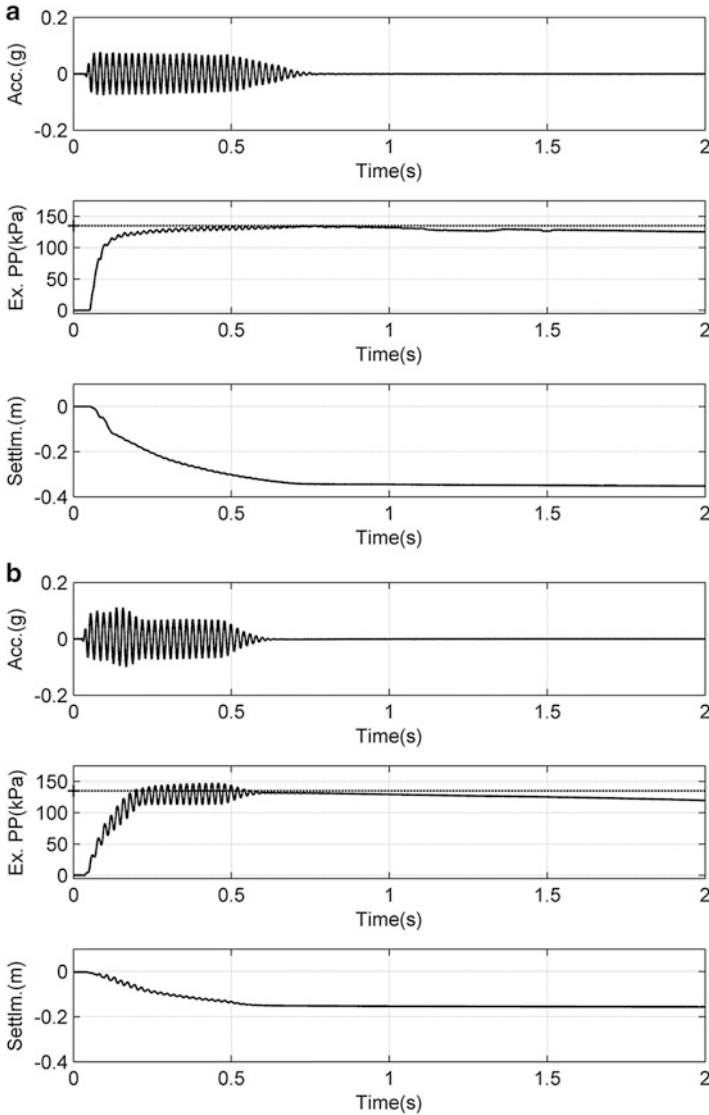lated for the liquefied soil in this period.

Fig. 16.16 Results from the centrifuge test on a soil model with a RD of 50% & 80% (**a**) RD = 50% (**b**) RD = 80%

16.4.1.2   Soil Settlements

In Fig. 16.16, the settlements suffered by loose and dense sands are presented. It can be seen that the loose sand suffers a total settlement of about 7 m while that for dense sand is less than half of this value being about 3 m. This is to be expected, as the dense sand suffers much smaller volumetric strains compared to loose sands even in the triaxial tests. In Fig. 16.16 it can also be seen that the rate of settlement is steepest

in the co-seismic period, reducing to a much smaller value in the post-seismic period. This is true for both loose and dense sands.

This observation is important, as settlement during the co-seismic period is only possible if the liquefied soil is not behaving in an undrained fashion. As these are level sand beds with no driving shear stresses induced by foundations etc., the rapid co-seismic settlements imply that some drainage of pore fluid is occurring to allow for the soil settlements. Thus the hypothesis of liquefaction being a partially drained event based on the soil stress state reaching the fracture line, as discussed in the previous section, is at least a plausible explanation for these rapid rates of settlement. A corollary to this observation is that thorough introspection is needed in using undrained cyclic triaxial tests to investigate the liquefaction behaviour of saturated sands.

Further, if one considers the soil stress state immediately after the end of the earthquake loading in Fig. 16.16, the excess pore pressures in the soil at this stage are still high and closely match the total stress. However, the rate of settlement changes abruptly after the end of the earthquake loading. Applying the definition given in Eq. 16.8, both soils are 'liquefied' at this stage. There must be a change in the behaviour of the soil to cause a change in the settlement rate. This aspect is further considered in developing a micro-mechanical model for soil liquefaction.

16.4.2 Shallow Foundations on Liquefiable Sand Beds

The problem of shallow foundations on liquefiable soil layers has been addressed by many researchers using dynamic centrifuge modelling before e.g. Mitrani and Madabhushi (2011), Marques et al. (2013). More recently Adamidis and Madabhushi (2017a) have investigated the effect of the thickness of liquefiable layers on shallow foundation behaviour (see Fig. 16.17). This is a relevant issue as many practical applications for shallow foundations encounter liquefiable layers where the thickness of these layers can be the order of the width of the foundation.

In Fig. 16.17 the cross-sectional view of two centrifuge models OA4 and OA6 with a shallow foundation supporting a single degree freedom structure is shown.
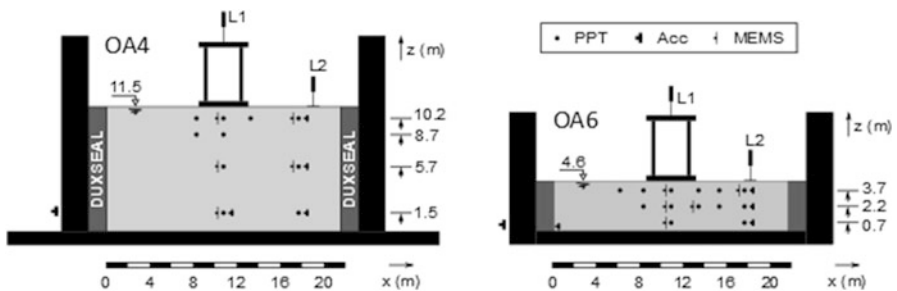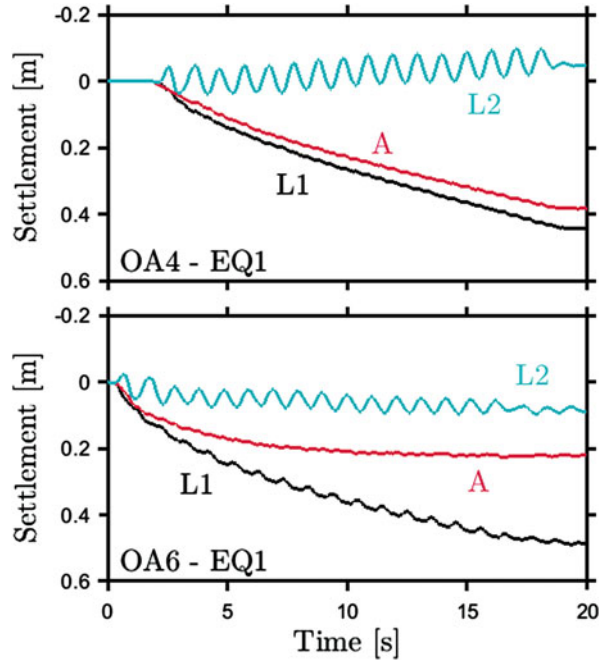

Fig. 16.17 Cross-section of centrifuge models with varying depths of liquefiable layers

Settlement [m]

OA4 - EQ1

L2

A

L1

Settlement [m]

OA6 - EQ1

L2

L1

A

Time [s]

The bearing pressure exerted by the foundation on the soil is ~50 kPa. The only
difference between these centrifuge models was the thickness of the liquefiable
layers. In Fig. 16.18 the settlement of the structure recorded in each centrifuge test
is presented during a sinusoidal earthquake with a peak bedrock acceleration of
0.23 g.

The settlement of the structure is given by L1 and that of the free field is given by
L2. 'A' gives the settlement of soil next to the foundation (obtained from PIV
analysis of images). In both centrifuge tests the foudation settles much more than
the free field during the co-seismic period. Surprisingly the magnitude of settlement
of structure given by L1 in both tests during this earthquake were quite comparable
(about 0.5 m) despite the differences in the thickness of the liquefiable layers. Free-
field settlement L2 shows some heave in test OA4 and some settlement in test OA6.
This suggests that the failure mechanism is wider in test OA4 and is much more
narrower and focused below the foundation in test OA6.

The differences in the deformation mechanisms that drove structural settlement
can be achieved by examining the total volumetric and shear strains at the end of
each event. Strains for tests OA4 and OA6 are depicted in Fig. 16.19. These were
calculated using the displacement fields computed through PIV (White et al. (2003)).
In these figures it can be seen that the volumetric strains, in general, are distributed
over the entire soil model. It can also be seen that the volumetric strains are larger at
the surface and reduce with depth. This is to be expected as the volumetric strains at
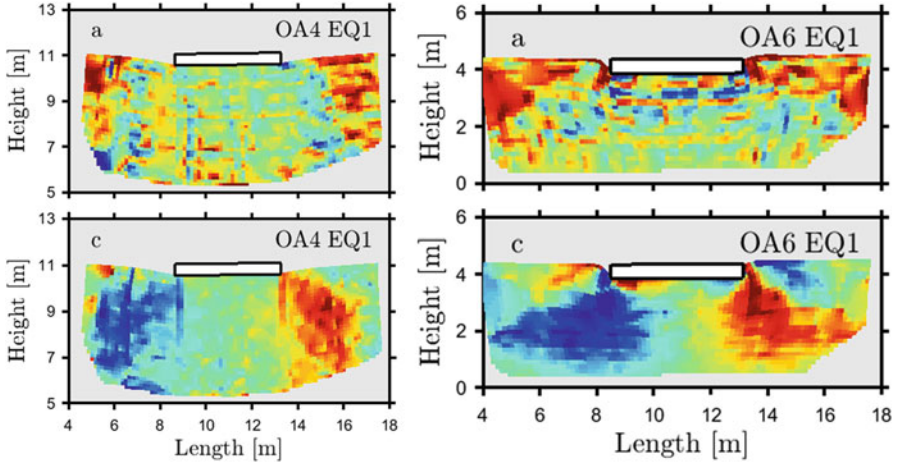the surface accumulate as one moves towards the surface. In contrast, the shear

Fig. 16.19 Volumetric and shear strains below foundation on deep liquefiable layer

strains are very sharply focused and emanate from the edges of the shallow founda-
tion, where one would anticipate the largest stress concentration. Further, the shear
strains are much larger and focused in test OA6 with a shallow depth of liquefiable
layer compared to the test OA4 that had a deeper soil layer. This also confirms the
earlier observation that the deformation mechanism is much more focused and
narrow in the case of a thin, liquefiable layer. More details of this set of tests can
be found in Adamidis and Madabhushi (2017a).

The main observation from these tests was that deformation of the liquefied soil
and the shallow foundation are governed by both volumetric strains and shear
strains. Presence of volumetric strains suggests that the liquefaction cannot be
treated as an 'undrained' event even in the co-seismic period.

16.4.3   Drainage During Liquefaction Events

Recently Adamidis and Madabhushi (2017b) have carried out novel centrifuge tests
in which an attempt was made to create 'triaxial' chambers within a centrifuge
model. This was done by having a latex membrane isolated zone of saturated soil as
shown in Fig. 16.20. Instrumentation such as accelerometers and pore pressure
transducers were used both within the triaxial chamber as well as the free-field. It
must be pointed out that this triaxial cell represents quite a large sample at prototype
scale. The soil was deposited at a relative density of ~40% and was saturated with
50 cS methylcellulose. The volume flow in and out of the triaxial chamber was
controlled through a valve system as shown in Fig. 16.20. Valves 1 and 2 are left
open during saturation of the model after which they were shut. During centrifuge
flight valve 1 was kept shut, but valve 2 was open after the end of the earthquake and
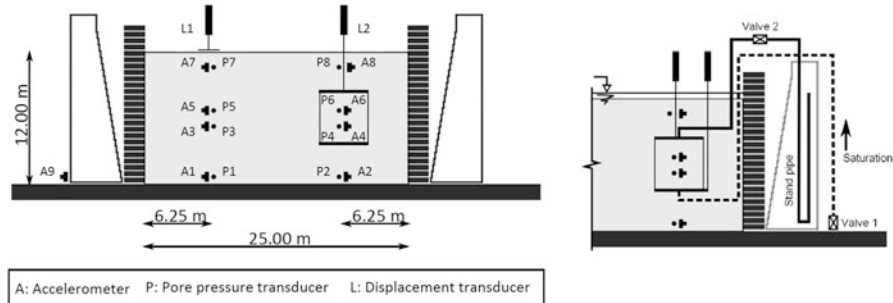
Fig. 16.20 Cross-section of a centrifuge model with enclosed 'triaxial cell'

any fluid outflow was monitored along with the settlement of the triaxial chamber. Two types of centrifuge tests were conducted. In the first case (test OA2) the triaxial cell had simple, latex boundary and therefore was able to expand laterally into the liquefied soil. In the second case (test OA3) the latex boundary was surrounded by very fine steel wire to prevent any lateral expansion of the triaxial cell. However, the triaxial cell is still able to suffer lateral contraction, if the soil behaviour dictated it. More details of the model preparation and testing can be found in Adamidis and Madabhushi (2017b). It must be pointed out that the data for these tests are shown at model scale.

16.4.3.1   Response of the Soil in the Triaxial Chamber & in the Free-Field

The excess pore pressure traces at different locations within the chamber and in the free-field are presented in Fig. 16.21 for the two tests OA2 and OA3 respectively along with the settlement data and the input accelerations applied at the bedrock level. The time scales on x-axis are partitioned to show initial cycles, co-seismic and post-seismic periods. For the centrifuge test OA2 shown in Fig. 16.21 the excess pore pressure build-up in the initial cycles is comparable between free-field and within the triaxial chamber. In the co-seismic period the free-field excess pore pressures are quite different at P3 & P5 locations, while those within the triaxial chamber quickly equalize. This is even clearer in the start of the post-seismic period. This is attributed to the drainage of pore fluid from the base of the model to the soil surface in the free-field which is maintained throughout the co-seismic period and also a few seconds into the post-seismic period. This is explained by using liquefaction and solidification front concepts by Adamidis and Madabhushi (2017a). Similar behaviour is also observed in test OA3 where the chamber is not allowed to bulge out into the liquefied soil. This slightly delayed the excess pore pressure equilibrating within the chamber as seen as a slow drop in excess pore pressure at P4 in Fig. 16.21.

In Fig. 16.21 the settlement of the triaxial chamber is also compared to the free-field settlements. In case of test OA2 we can see that the chamber settles a lot less
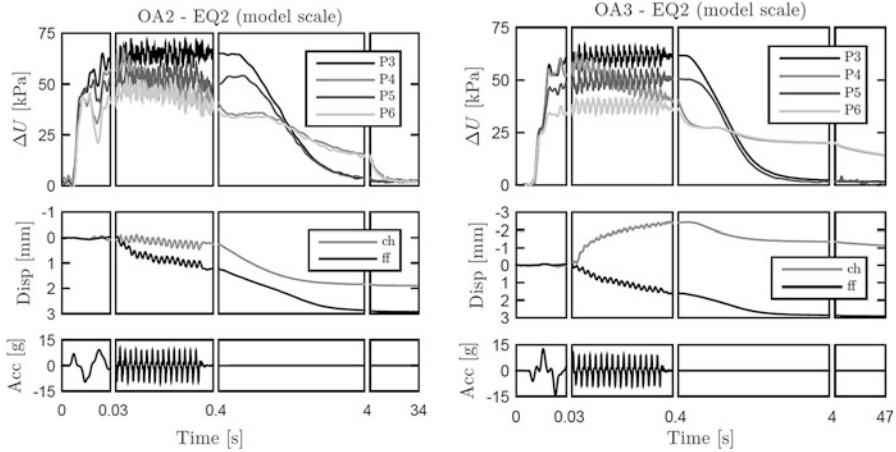
Fig. 16.21 Response in the free-field and in the triaxial chamber in test OA2 & OA3

than the free-field even in the co-seismic period. This again emphasizes the importance of drainage during earthquake loading, which is prevented artificially in a triaxial chamber. For test OA3, which is constrained from expanding laterally outwards, the free-field settles as before but the triaxial chamber actually heaves up. This is due to the radial compression of the chamber by the liquefied soil outside the chamber causing a rise in the top cap due to 'constant volume' condition that was imposed artificially.

16.4.3.2 Stress-Strain Behaviour of Liquefied Soil in the Chamber & in the Free-Field

The stress-strain behaviour of liquefying sands can also be obtained in these centrifuge tests from the acceleration-time histories measured in the free-field and in the chamber. The shear stress and shear strain plots for tests OA2 and OA3 are shown in Fig. 16.22. In Fig. 16.22c the τ–σ'_v plot is shown for the whole earthquake loading period from starting circles to finishing squares, for both free-field and in the chamber. Similarly Fig. 16.22d and e show the τ–γ plot for the initial cycles (left) and post liquefaction (right). Equivalent plots for test OA3 with constrained lateral boundary for the triaxial chamber are also shown in Fig. 16.22. In this test the drop in shear strains in the free-field relative to the chamber (see Fig. 16.22) is even more significant clearly suggesting the drop in shear stiffness in the free field is far more than in the chamber. Overall the stress paths in Fig. 16.22 for OA2 and OA3 tests are very different as are the stress-strain plots.

These comparisons shows quite clearly that by creating and using triaxial samples to study liquefaction, different behaviour can be elicited by imposing different drainage boundary conditions and by imposing radial constraints against lateral
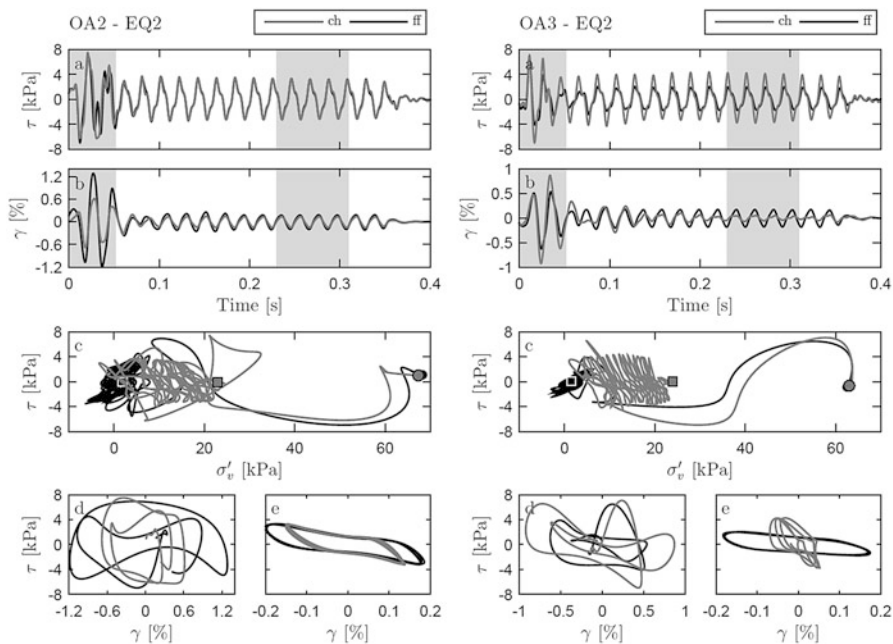
Fig. 16.22 Stress-strain plots in test OA2 & OA3

expansion of the triaxial chamber. The soil in the free field seems to suffer a greater degradation in its stiffness compared to the soil enclosed in the triaxial chamber.

16.4.4   Novel Liquefaction Mitigation Methods

Liquefaction mitigation methods of various kinds have been investigated previously in Cambridge. The efficacy of drains in relieving the excess pore pressures was investigated by Brennan and Madabhushi (2005). Similarly use of impermeable barriers or solidification of liquefiable sands using cementation was investigated by Mitrani and Madabhushi (2013). In a very recent study at Cambridge, liquefaction mitigation was attempted by partially saturating a sand bed, Zeybek and Madabhushi (2016, 2017). This was achieved by using in-flight air injection at the base of the soil model as shown in Fig. 16.23. A shallow foundation was placed at the soil surface that applied a bearing pressure of ∼ 50 kPa. The soil was saturated using 50 cS methylcellulose as usual as the centrifuge testing was carried out at 50 g's. A bench mark test FS-1 was first conducted with no air injection. This was followed by two other tests PS-1 and PS-2 in which high pressure air was injected into the soil to cause partial saturation. This was carried out over a period of about 180 seconds. Different types of injection devices were used in tests PS-1 and PS-2. Using digital imaging obtained for PIV analysis, it was possible to perform further digital image
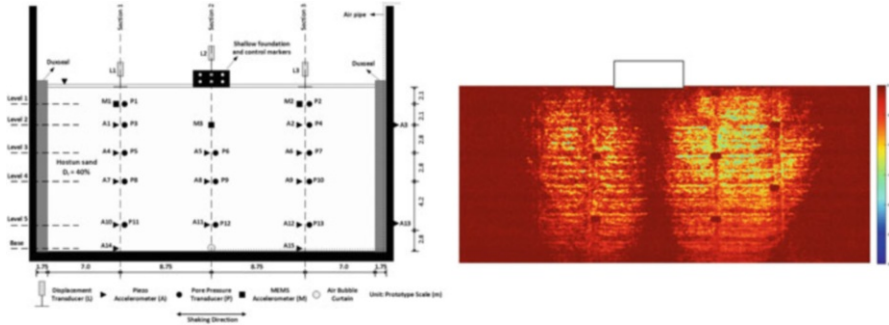
Fig. 16.23 Cross-section of the centrifuge model with air injection & image analysis showing air-injected region below the foundation
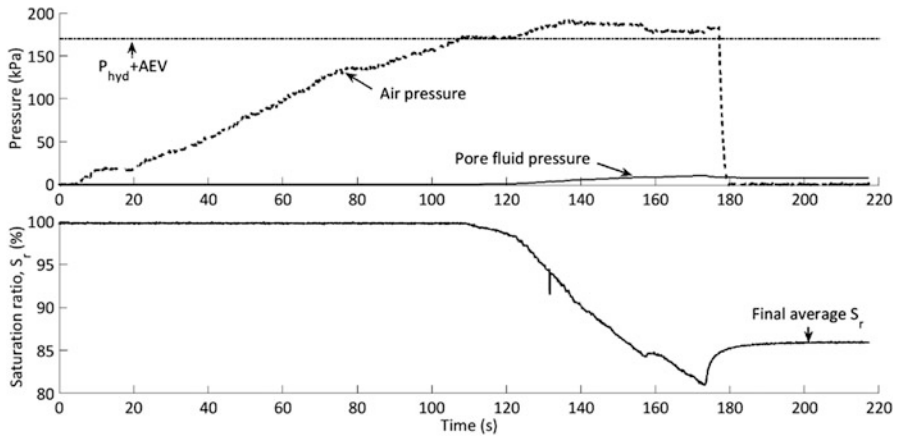

Fig. 16.24 Changes in degree of saturation during air injection

analysis to observe the areas of the foundation soil affected by air-injection. In Fig. 16.23, an example showing the region into which air-injection took place is shown (lighter yellow indicates more air presence.

In this testing program, the first step was the air injection prior to application of any earthquake loading. The centrifugal acceleration was increased to reach 50 g's. At this stage high pressure air was injected at the base of the soil model. Details of the air injection system are described by Zeybek and Madabhushi (2016). Also the results from these tests are shown at prototype scale. In Fig. 16.24 the increase in air pressure is plotted along with the decrease in the degree of saturation. In this figure it can be seen that the degree of saturation drops from 100% to about 81% during air injection, before recovering slightly to a value of 85%.

Soon after the air injection process was completed earthquake loading was applied. In Fig. 16.25 the response recorded by the pore pressure transducers is

plotted both below the structure and in the free-field. In this figure it can be seen that while the bench mark test FS-1 shows full levels of liquefaction both PS-1 and PS-2 show much lower levels of excess pore pressure generation both at shallow level and deep level. The settlement suffered by the shallow foundation in each test are also plotted in Fig. 16.25 (note +displacement is taken as settlement in this plot). The settlements observed in this 0.2 g earthquake are seen to be much smaller in the air injected models PS-1 and PS-2 (about 40 mm settlement) compared to the fully saturated case of FS-1 (about 750 mm settlement). Also the air injection device in PS-2 worked better than in the case of PS-1.

It can therefore be concluded that the air-injection and subsequent drop of degree of saturation by about 15%, has successfully reduced the settlement suffered by the shallow foundation. In these tests high speed imaging was carried out during earthquake loading and resulting images were analysed using the geo-PIV software. This produces the displacement vectors below the shallow foundation as shown in Fig. 16.26. In this figure a direct comparison of the deformation suffered in each of the centrifuge tests are presented. It can be seen in this figure that the benchmark case
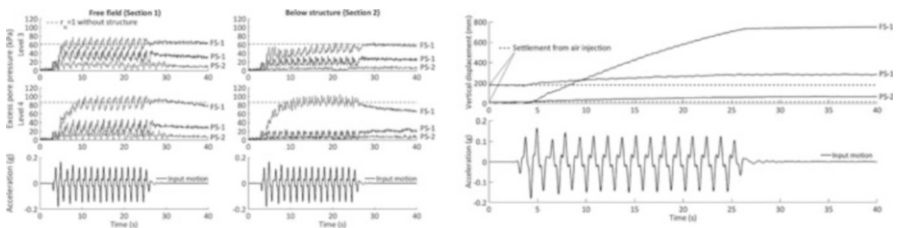

Fig. 16.25 Excess pore pressures & settlements in bench mark test (FS-1) and the air-injection tests (PS-1 and PS-2)
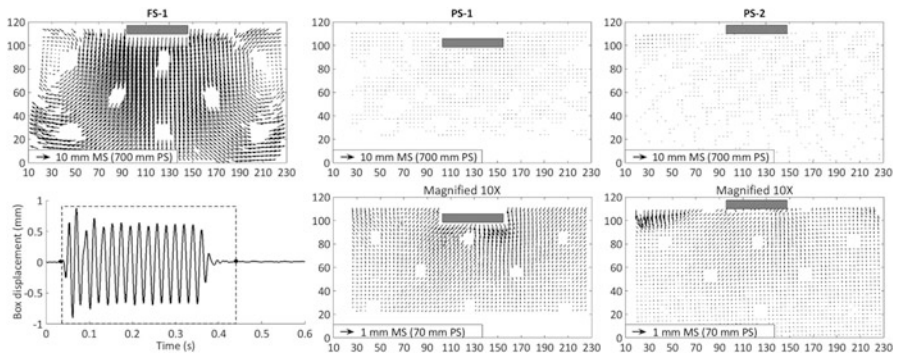

Fig. 16.26 Soil deformations below the foundation in the bench mark test (FS-1) and the air-injection tests (PS-1 & PS-2). Note the deformations in second row are magnified by ×10

of FS-1 shows enormous deformations as the foundation settles by 750 mm following soil liquefaction. In comparison for the centrifuge tests PS-1 and PS-2 the deformations are barely noticeable. In fact in the second row of this figure the deformations are magnified by a factor of ×10 and replotted to reveal the deformations. In these second row figures the deformations become more visible. For the case of PS-1, one can decipher a bearing capacity failure type mechanism evolving. For the case of PS-2 the deformations are still small and this figure is dominated by the free-field settlements on the left hand corner. It must be pointed that the PIV field shown here is much smaller than the actual soil sample shown in Fig. 16.26. This is due to the limited visual field of the high speed camera.

16.5   Conclusions

Liquefaction of soil following earthquake events continue to have serious consequences to civil engineering infrastructure. Research into soil liquefaction and development of theoretical frameworks is predominantly driven by observations from cyclic triaxial testing while dynamic centrifuge tests continue to provide new and more detailed information on liquefaction phenomena. In this paper the basic assumption that liquefaction events are largely undrained is questioned. Earlier work at Cambridge has shown that the permeability and compressibility of sands under low effective stresses can increase significantly. This leads to drainage of liquefied sands during the earthquake loading events. Dynamic centrifuge test data from tests on level beds of sand confirm that the excess pore pressure generation is similar for loose and dense sands but the settlements are much lower for dense sands. This can be attributed to the fact that loose sands when liquefied are much more compressible than dense sands. Also the majority of settlements occur during the co-seismic period confirming increased permeability and a consequent drainage occurring even in the co-seismic period. Recent centrifuge testing conducted at Cambridge on shallow foundations on liquefiable layers of different thicknesses show that both volumetric and shear strains occur below shallow foundations once the ground has liquefied.

Novel experiments were also conducted on level beds of sand in which a 'triaxial chamber' was created within the centrifuge model. It was shown that the behaviour of liquefied sand within the chamber is very different to that in the free-field. This illustrates the importance of drainage in the co-seismic period. Further the centrifuge data was also used to show the post-liquefaction reconsolidation process and the changes in permeability and compressibility of sands during this period. Finally, the dynamic centrifuge testing was used to investigate the efficacy of air injection to reduce the liquefaction potential of soils. The data from this series of tests show that injection of air reduces both the excess pore pressure generation and consequently the settlement of shallow foundations on such partially saturated sands. The deformation mechanisms obtained through PIV analysis also confirm the reduced settlement of such foundations.

References

Adamidis O, Madabhushi SPG (2015) Use of viscous pore fluids in dynamic centrifuge modeling. Int J Phys Modell Geotech 15(3):141–149

Adamidis O, Madabhushi GSP (2016) Post-liquefaction reconsolidation of sand. Proc R Soc A Math Phys Eng Sci 472:20150745. https://doi.org/10.1098/rspa.2015.0745

Adamidis O, Madabhushi GSP (2017a) Deformation mechanisms under shallow foundations resting on liquefiable layers of varying thickness, Geotechnique, Thomas Telford, https://doi.org/10.1680/jgeot.17.P.067

Adamidis O, Madabhushi GSP (2017b) Drainage during earthquake-induced liquefaction, Geotechnique, Thomas Telford, https://doi.org/10.1680/jgeot.16.p.090

Brennan AJ, Madabhushi SPG (2005) Liquefaction and drainage in stratified soil. ASCE J Geotech Geo Environ Eng 131(7):876–885

Brennan AJ, Madabhushi SPG (2011) Measurement of coefficient of consolidation during reconsolidation of liquefied sand. ASTM Geotech Test J 34(2):64–72

Brennan AJ, Madabhushi SPG, Houghton NE (2006) Comparing laminar and ESB Containers for Dynamic Centrifuge Modelling. Proceedings of Centrifuge'06, International Conference on physical modelling, Hong Kong

Casagrande A (1936) Characteristics of cohesionless soils affecting the stability of slopes and earth fills. J Boston Soc Civil Eng. pp 257–294

Casagrande A (1971) On liquefaction phenomena. Reprinted in Geotechnique 21(3)

Castro G (1969) Liquefaction of sands. PhD Thesis, Harvard University. Reprinted as Hazard Soil Mechanics Series (8):l–112

Chian S, Tokimatsu K, Madabhushi S (2014) Soil liquefaction–induced uplift of underground structures: physical and numerical modeling. ASCE J Geotech Geoenviron Eng 140 (10):04014057

Cilingir U, Madabhushi SPG (2011) A model study on the effects of input motion on the seismic behaviour of tunnels. J Soil Dyn Earthq Eng 31:452–462

Coelho PALF, Haigh SK, Madabhushi SPG, O'Brien AS (2007) Post-earthquake behaviour of footings when using densification as a liquefaction resistance measure. Ground Improv J 11 (1):45–53

Dixon SJ, Burke JW (1973) Liquefaction case history. ASCE J Soil Mech Found Eng SM10:823-840

Ghosh B, Madabhushi SPG (2007) Centrifuge modelling of seismic soil-structure interaction effects. J Nucl Eng Des 237:887–896

Haigh SK, Eadington J, Madabhushi SPG (2012) Permeability and stiffness of sands at very low effective stresses. Geotechnique 62(1):69–75

Knappett JA, Madabhushi SPG (2009) Seismic bearing capacity of piles in liquefiable soils. Soils Found 49(4):525–536

Kramer SL (1996) Geotechnical earthquake engineering. Prentice Hall Inc., Upper Saddle River. ISBN 013374943-6

Madabhushi SPG (2014) Centrifuge modelling for civil engineers. CRC Press, London. 9780415668248

Madabhushi SPG, Haigh SK (2009) Effect of superstructure stiffness on liquefaction-induced failure mechanisms. Int J Geotech Earthq Eng 1(1):72–88

Madabhushi SPG, Schofield AN, Lesley S (1998) A new stored angular momentum (SAM) based earthquake actuator. Proceedings of Cenrifuge'98, International conference on Centrifuge Modelling, Tokyo, Japan

Madabhushi SPG, Patel D, Haigh SK (2005) Geotechnical aspects of the Bhuj earthquake, Chapter 3, EEFIT Report, Institution of Structural Engineers, London. ISBN 0901297 372

Madabhushi SPG, Haigh SK, Houghton NE, Gould E (2012) Development of a servo-hydraulic earthquake actuator for the Cambridge turner beam centrifuge. Int J Phys Modell Geotech 12 (2):77–88

Marques ASP, Coelho PALF, Haigh SK, Madabhushi SPG (2013) Centrifuge modelling of liquefaction effects on shallow foundations. Special edition on seismic evaluation and rehabilitation of structures. In: Ilki A, Fardis MN (eds) Geotechnical, geological and earthquake engineering, vol 26. Springer, Dordrecht, pp 425–441

Mitrani H, Madabhushi SPG (2011) Rigid containment walls for liquefaction remediation. J Earthq Tsunami 6(3). https://doi.org/10.1142/S1793431112001309

Mitrani H, Madabhushi SPG (2013) Geomembrane containment walls for liquefaction remediation. Proc ICE Ground Improv J 166(GI1):9–20

Muhunthan B, Schofield AN (2000) Liquefaction and dam failures. Proceedings of *GeoDenver*, Denver, Colorado, USA

Roscoe KH, Schofield AN, Wroth CP (1958) On the yielding of soils. Geotechnique 8:22–53

Schofield AN (1980) Cambridge geotechnical centrifuge operations. Geotechnique 25(4):743–761

Schofield AN (1981) Dynamic and earthquake geotechnical centrifuge modelling. Proceedings International conference on recent advances in geotechnical earthquake engineering and soil dynamics, St Louis, vol III, pp 1081–1100

Schofield AN, Wroth CP (1968) Critical state soil mechanics. McGraw-Hill, London

White DJ, Take WA, Bolton MD (2003) Soil deformation measurement using particle image velocimetry (PIV) and photogrammetry. Géotechnique 53(7):619–663

Zeng X, Schofield AN (1996) Design and performance of an equivalent-shear-beam container for earthquake centrifuge modelling. Géotechnique 46(1):83–102

Zeybek A, Madabhushi SPG (2016) Effect of bearing pressure and degree of saturation on the seismic liquefaction behaviour of air-induced partially saturated air-sparged soils below shallow foundations. Bull Earthq Eng 15:339. https://doi.org/10.1007/s10518-016-9968-6

Zeybek A, Madabhushi SPG (2017) Influence of air injection on the liquefaction-induced deformation mechanisms beneath shallow foundations. J Soil Dyn Earthq Eng 97:266–276